

Time-dependent MHD shocks and line intensity ratios in the HH 30 jet: A focus on cooling function and numerical resolution

O. Teșileanu^{1,2}, S. Massaglia², A. Mignone², G. Bodo³, and F. Bacciotti⁴

¹ RCAPA - Department of Physics, University of Bucharest, CP MG-11, RO-077125, București-Măgurele, Romania

² Dipartimento di Fisica Generale dell'Università, Via Pietro Giuria 1, I-10125 Torino, Italy
email: tesilean@ph.unito.it, massaglia@ph.unito.it, mignone@ph.unito.it,

³ INAF - Osservatorio Astronomico di Torino, Viale Osservatorio 20, I-10025 Pino Torinese, Italy
email: bodo@to.astro.it

⁴ INAF - Osservatorio Astrofisico di Arcetri, Largo E. Fermi 5, I-50125 Firenze, Italy
email: fran@arcetri.astro.it

Received; accepted

ABSTRACT

Context. The coupling between time-dependent, multidimensional MHD numerical codes and radiative line emission is of utmost importance in the studies of the interplay between dynamical and radiative processes in many astrophysical environments, with particular interest for problems involving radiative shocks. There is a widespread consensus that line emitting knots observed in Herbig-Haro jets can be interpreted as radiative shocks. Velocity perturbations at the jet base steepen into shocks to emit the observed spectra. To derive the observable characteristics of the emitted spectra, such as line intensity ratios, one has to study physical processes that involve the solution of the MHD equations coupled with radiative cooling in non-equilibrium conditions.

Aims. In this paper we address two different aspects relevant to the time-dependent calculations of the line intensity ratios of forbidden transitions, resulting from the excitation by planar, time-dependent radiative shocks traveling in a stratified medium. The first one concerns the impact of the radiation and ionization processes included in the cooling model, and the second one the effects of the numerical grid resolution.

Methods. Dealing with both dynamical and radiative processes in the same numerical scheme means to treat phenomena characterized by different time and length scales. This may be especially arduous and computationally expensive when discontinuities are involved, such as in the case of shocks. Adaptive Mesh Refinement (AMR) methods have been introduced in order to alleviate these difficulties. In this paper we apply the AMR methodology to the treatment of radiating shocks and show how this method is able to vastly reduce the integration time.

Results. The technique is applied to the knots of the HH 30 jet to obtain the observed line intensity ratios and derive the physical parameters, such as density, temperature and ionization fraction. We consider the impact of two different cooling functions and different grid resolutions on the results.

Conclusions. We conclude that the use of different cooling routines has effects on results whose weight depends upon the line ratio considered. Moreover, we find the minimum numerical resolution of the simulation grid behind the shock to achieve convergence in the results. This is crucial for the forthcoming 2D calculations of radiative shocks.

Key words. ISM: jets and outflows – (ISM): Herbig-Haro objects – Magnetohydrodynamics (MHD) – Shock waves – Methods: numerical

1. Introduction

Supersonic flows are ubiquitous in the Universe: expanding supernova remnants, stellar winds, AGN and Herbig-Haro jets are some examples, and shocks are abundant and prominent in these flows. Shocks located in extragalactic environments, such as AGN jets, can be considered adiabatic, since the cooling time for thermal emission typically exceeds by far the source lifetime. On the other hand, shocks that form in galactic objects such as supernova remnants and Herbig-Haro jets must be treated including radiative effects.

Radiative shocks have been studied in steady-state conditions by several authors (e.g. Cox & Raymond 1985, Hartigan et al. 1994), who derived the one-dimensional post-shock behavior of various physical parameters (temperature, ionization fraction, electron density, etc.), as functions of the distance from the shock front. From these studies it turns out that the physical parameters vary behind the shock front on scale lengths

that differ by orders of magnitude, and this becomes a major problem when tackling the time-dependent evolution of such radiative shocks. For example, in Herbig-Haro jets, one needs to treat in the same scheme spatial scales well below $\sim 10^{13}$ cm, to reproduce the time-dependent post-shock temperature variations correctly, and scales $\leq 10^{15}$ cm to study the behavior of the electron density (Massaglia et al. 2005a, Paper I). Under these conditions and with these requirements, employing an Adaptive Mesh Refinement (AMR) technique becomes almost mandatory. This technique can provide adequate spatial and temporal resolution by dynamically adapting the grid to the moving regions of interest, giving a tremendous saving in computational time and memory overhead with respect to the more traditional uniform grid approach.

The important issue of numerical spatial resolution in time-dependent simulations of radiative shocks in 2D has been considered by Raga et al. (2007) employing an AMR technique as well. They discussed the dependence of the morphological struc-

ture of the perturbations depending on the grid resolution. Their maximum grid resolution was with a cell size corresponding to 1.5×10^{12} cm. They found that while the detailed structure of the shocks depends on the resolution, the emission line luminosities, integrated over the volume, are less dependent on cell size.

A second crucial question is: does the dependence on the cooling function details have qualitative or quantitative effects on the calculated distributions of the physical parameters? Teşileanu et al. (2008) have developed a detailed treatment including an ionization network of 29 species and compared, at constant numerical resolution, the resulting distribution of physical parameters (such as temperature, density, etc.) with the one obtained employing the simplified cooling of Paper I, for a 2D cylindrical jet affected by perturbations that evolved in internal working surfaces. They found quantitative differences but qualitatively the outcomes were very similar.

A more challenging problem than the determination of the integrated line emissions and distributions of physical parameters is the calculation of line intensity ratios between different species. In this case, the fractional abundances of the various species vary in very different ways with space behind the shocks (see Paper I). This variation is mainly governed by the temperature profile, which is typically a very steep function of space. Therefore we will examine the effects of both the details of the cooling function and of the grid resolution adopted.

As discussed in Paper I and Massaglia et al. (2005b), observations of some HH jets at distances of a few arcseconds from the source typically show that the behavior of temperature, ionization and density along the jet is incompatible with a freely cooling jet. It is now generally accepted that the line emission in HH jets is a result of the observation of several post-shock regions of high excitation with a filling factor of about 1%. In our calculations, we will refer, in particular, to the observational results described in Bacciotti et al. (1999), where a specialized diagnostic technique has been applied to HST data of the HH 30 jet. Hartigan & Morse (2007) also re-examined the HH 30 case using slitless spectroscopy performed with the Hubble Space Telescope Imaging Spectrograph. Their results are fully consistent with the findings in Bacciotti et al. (1999).

In this paper, we will follow the dynamical evolution of an initial perturbation as it steepens into a (radiative) shock traveling along the jet, and derive the post-shock physical parameters consistently. From these parameters, we construct the synthetic theoretical emission line ratios to be compared with observations. Using this setup, we implicitly consider that the medium in the real jet returns close to the steady jet conditions between the propagating shocks. This was verified in parallel 2D simulations (Teşileanu et al. 2009), as the 1D simulation, being done in the reference frame of the mean flow, lacks the steady flow of the jet. After the shock and the high-density post-shock zone pass, there follows an underdense zone, and then the medium returns to the stationary conditions of the constant flow. The distance after which this happens increases during the evolution of the shock from 0.5×10^{14} cm close to the jet base to about 10^{15} cm at 500 AU from the base. This increasing distance becomes resolved observationally at about 200 AU from the base of the jet, and also at such distances interactions between different shockwaves become likely, these being possible explanations for the oscillations visible in the observational data after 200 AU. The emission at each point of the jet is computed by simulating the propagation of a shock produced at the base of the jet up to that point. As discussed before, we will adopt two different treatments for the radiative losses, namely: i) the simplified cooling

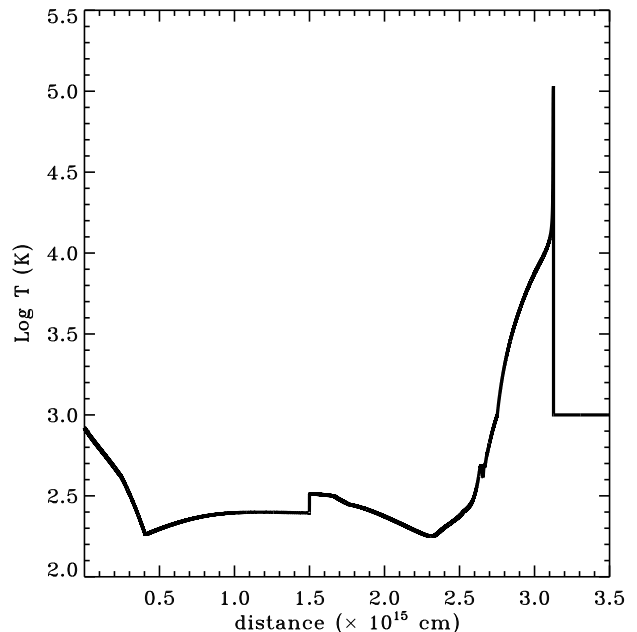


Fig. 1. Snapshot of the temperature behavior vs distance for the uniform grid, for a propagating shock in a stratified medium.

employed in Paper I and ii) the new cooling treatment described in Teşileanu et al. (2008).

The plan of the paper is the following: In Section 2 we present the computation setup and the adopted techniques to model the problem; in Section 3 we apply the model to the case of HH 30 and discuss the results obtained with the two cooling functions and the effects of the grid resolution; the conclusions are drawn in Section 4.

2. The model

In this Section we give a general outline of the model and the form of the initial perturbation. More details on the setup can be found in Paper I, where we analyzed the case of the DGTau jet.

As mentioned in the Introduction, in the preshock conditions assumed here (decreasing density departing from a few 10^4 cm^{-3} , uniform temperature of 2000 K) the post-shock temperature drops by about one order of magnitude over a scale length lower than $\sim 10^{13}$ cm i.e. a much smaller distance than the post-shock evolution that goes on over distances of a few times 10^{15} cm. This has been a compelling reason for developing and employing Adaptive Mesh Refinement, as in Paper I, described in detail in a companion paper (Mignone et al. 2009). We have verified the validity of this approach by computing several of the models presented in the next section on uniform and adaptive meshes and found a tremendous gain in efficiency. Figs. (1) and (2) show the results of one particular model computed on a uniform grid employing 49152 zones and on an equivalent adaptive grid with 5 levels of refinement (base level resolution is 1536 zones). On a Pentium IV processor with a 1.7 GHz clock and 1 GB of RAM, the uniform grid approach took about 6.04×10^4 sec, while the AMR computation required only 238 sec, up to the same final integration time $t = 5 \times 10^3$.

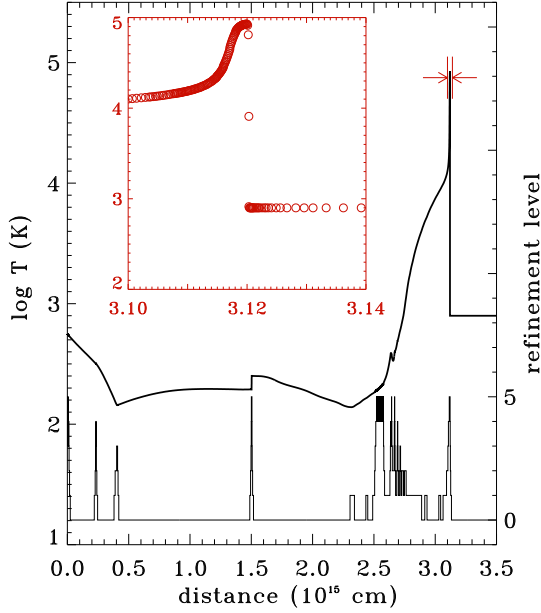


Fig. 2. The same as in Fig. 1 but for the AMR integration and five levels of refinement, for an equivalent resolution of 49152 cells, with a zoom on the shock region. The histogram in the lower part of the plot (with the right vertical scale) represents the refinement level employed in each cell of the simulation.

2.1. Model equations and initial perturbation

We restrict our attention to one-dimensional MHD planar flow, which implies that we are following the shock evolution along the jet axis. The fluid is described in terms of its density ρ , velocity u , thermal pressure p and (transverse) magnetic field B_y . These quantities obey the standard MHD equations for conservation of mass, momentum, magnetic field and total energy, in the presence of radiative cooling represented by the energy loss term $\mathcal{L}(T, \mathbf{X})$ (energy per unit volume per unit time), which depends on the temperature T and on the ionization state of the plasma, described by the vector of ionization fractions \mathbf{X} . A discussion on the cooling function follows in the next subsection.

A nonuniform preshock density that decreases away from the star is a reasonable assumption when dealing with an expanding jet, as suggested by observations. We note that shocks propagating into a stratified medium tend to increase their amplitude when they find a decreasing preshock density. We consider the following form for the preshock density:

$$\rho_0(x) = \rho_0 \frac{x_0^p}{x_0^p + x^p}. \quad (1)$$

where x is the spatial coordinate along the jet axis, x_0 sets the initial steepness of the density function (this affects the shock evolution even at larger distances) and $1 \leq p \leq 2$.

As in Paper I, the form of the initial perturbation has been taken in such a way as to keep the hydrodynamic Riemann invariant $J_- = \text{constant}$. In this way a single forward shock is formed. In this scheme, the density perturbation is:

$$\rho = \left[\frac{\gamma - 1}{2\sqrt{K}\gamma} (u - U_0) + \rho_0^{\frac{\gamma-1}{2}} \right]^{\frac{2}{\gamma-1}}, \quad (2)$$

where K is a constant derived from the single shock assumption, $\gamma = 5/3$ (the gas is monoatomic; molecules form at lower temperatures, while we are interested in the post-shock regions of high radiative emission), U_0 is the mean flow velocity and the initial velocity perturbation is:

$$u(x) = \begin{cases} u_0[-(x - x_1)^2 + 2\sigma(x - x_1)] & \text{if } 2\sigma + x_1 > x > x_1 \\ 0 & \text{otherwise} \end{cases}$$

where u_0 is the perturbation amplitude, x_1 is the initial coordinate of the perturbation and σ is its half-width. However, the exact shape of the perturbation is not crucial for the model. In our calculations we take $x_1 = 10^{14}$ cm and $\sigma = 2 \times 10^{13}$ cm.

In carrying out the calculations we have set $U_0(x) = 0$, i.e. the reference frame is that of the mean flow (that is, the steady jet flow on which the perturbation is set). To transform the results back to the laboratory frame we have set $U_0 = 100$ km s $^{-1}$, which is the bulk velocity we assume for the HH 30 jet (U_0 must not be mistaken for u_0 , the initial velocity perturbation amplitude).

The boundary conditions assume free outflow at $x = 0$ and $x = L$. The extent of the computational domain, L , has been chosen sufficiently large to follow the shock evolution for $t \sim 15$ yrs and to avoid spurious interactions with the boundaries. For this reason, we adopt $L = 4.5 \times 10^{15}$ cm.

The assumption of a monoatomic gas is justified in the case of HH30 and many other YSO jets – however, there are cases (the so-called “molecular jets”) when this assumption is not valid anymore, and molecular cooling must be taken into account.

2.2. Radiative cooling

In the current work we use two different approaches for the computation of the radiative cooling loss term $\mathcal{L}(T, \mathbf{X})$. In a first simplified model (see Paper I), \mathbf{X} consists of the ionization fraction of H only, whereas a second, more accurate treatment is summarized below.

In the detailed cooling treatment, described in Teşileanu et al. (2008), 28 additional evolutionary equations are solved for the non-equilibrium ionization fractions \mathbf{X} (of H, He, C, N, O, Ne and S). The loss term accounts for energy lost in lines as well as in the ionization and recombination processes. Line emissions include contributions from transitions of the 29 ion species. The metal abundances are the ones adopted by Bacciotti et al. (1999), in particular $N/H = 1.1 \times 10^{-4}$, $O/H = 6 \times 10^{-4}$, $S/H = 1.6 \times 10^{-5}$ and the abundance of C is 10% of the solar one.

To carry out comparisons between the observed and computed line intensity ratios, we have determined the populations of the atomic levels relevant for [SII], [NII] and [OI] emission, solving the excitation - de-excitation equilibrium equations for five energy levels, according to Osterbrock & Ferland (2006). The line emissions reported in Bacciotti et al. (1999) for the HH 30 jet are: [SII] $\lambda 6716 + \lambda 6731$, [NII] $\lambda 6548 + \lambda 6583$ and [OI] $\lambda 6300$, and the corresponding intensity ratios [OI]/[NII] and [SII]/[OI].

3. The case of the HH 30 jet

To illustrate the astrophysical application of the above methodology, we will apply it to the numerical simulation of some of the physical properties of the HH 30 jet.

We have integrated the magneto-fluid equations employing the AMR method described previously with eight levels of refinement, using the PLUTO code (Mignone et al. 2007). As in

Paper I, in order to obtain values directly comparable with observations, we have space averaged all post-shock quantities at each evolutionary time point:

$$\langle Q(t) \rangle = \frac{\int Q(x, t) \epsilon\{[SII](x, t)\} dx}{\int \epsilon\{[SII](x, t)\} dx} \quad (3)$$

where $Q(x, t)$ is a physical quantity such as electron density or ionization fraction or temperature. This procedure is applied because by processing the observational data, we only have access to the physical parameters of the line-emitting regions, so this weighting is implicit. Differently from Paper I, where we averaged the line intensity ratios using the total line emissivity of the corresponding emitters as weighting functions, in the present paper we find the unweighted average of the line emissivity and calculate the ratio of the average lines afterward. This procedure does not lead to results that differ qualitatively from the previous ones, but appears closer to the actual observation process. To calculate the line emissivities, the atomic transition rates and collision strengths adopted are the ones described in Teşileanu et al. (2008). The collision strengths have been interpolated using a Lagrangian scheme to account for their temperature dependence.

The main free parameters of the model are: the particle density (at $x = 0$) n_0 , x_0 , the velocity perturbation amplitude u_0 and initial transverse magnetic field B_0 . Taking advantage of the peculiar efficiency of the AMR method, we have widely explored this parameter space to find good agreement with the observed line ratios. We have set the (uniform) preshock temperature $T_0 = 1,000$ K and the initial ionization fraction $f_i = 0.1\%$, i.e. due to the metal contribution only.

Both radiative cooling treatments were employed in the simulations, searching for the best agreement of the model results with the observations for each one. A discussion of the differences in the results follows.

3.1. Simplified cooling

The simplicity of this cooling model allows for rapid simulations, and thus the very efficient exploration of the parameter space. The root mean square deviations of the simulated line ratios with respect to the observational ones were computed (a few examples are shown in Table 1) in order to quantitatively estimate how close each simulation is to observations. The simulations presented in the table have base densities of $2 \times 10^4 \text{ cm}^{-3}$ (n2e4) or $5 \times 10^4 \text{ cm}^{-3}$ (n5e4), transverse magnetic field $300 \mu\text{G}$ (b300) or $500 \mu\text{G}$ (b500), and amplitude of the perturbation in velocity 50 (v50), 55 (v50) and 70 km s^{-1} (v70).

Simulation	[OI]/[NII]	[SII]/[OI]
n5e4b500v70	0.440	0.305
n2e4b500v55	0.161	0.103
n5e4b500v55	0.121	0.143
n2e4b500v50	0.068	0.110
n2e4b300v50	0.063	0.108

Table 1. Root mean square deviations of line ratios with simplified cooling.

A combination of the parameters that yielded a reasonably good agreement with the observed line intensity ratios, employing the simplified cooling model, was $n_0 = 2 \times 10^4 \text{ cm}^{-3}$, $B_0 = 300 \mu\text{G}$, $x_0 = 0.''1$ and $u_0 = 50 \text{ km s}^{-1}$. In Paper I

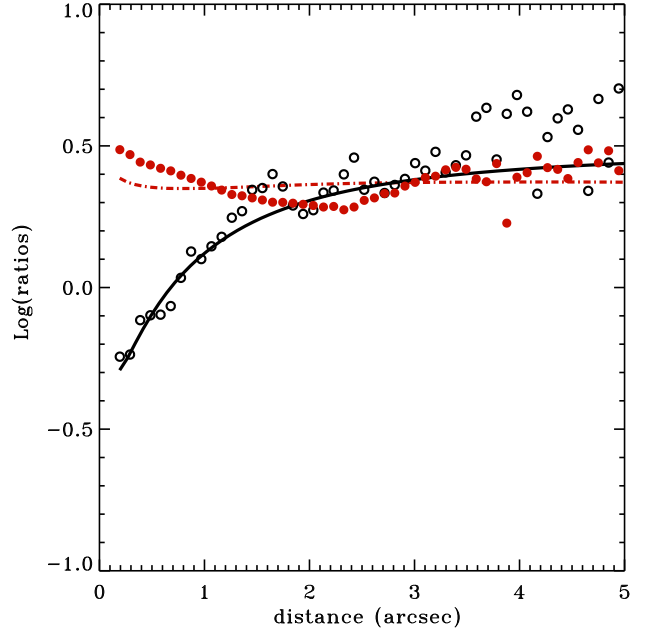


Fig. 3. Intensity ratios of $[SII]\lambda 6716 + \lambda 6731$, $[NII]\lambda 6548 + \lambda 6583$ and $[OI]\lambda 6300$ lines vs distance. Symbols represent the data from Bacciotti et al. (1999) and curves are the computed model curves (using the *simplified cooling* model): $[OI]/[NII]$ (bullets, dot-dashed line) and $[SII]/[OI]$ (circles, solid line). The model parameters are $n_0 = 2 \times 10^4 \text{ cm}^{-3}$, $B_0 = 300 \mu\text{G}$, $x_0 = 0.''1$ and $u_0 = 50 \text{ km s}^{-1}$, with $U_0 = 100 \text{ km s}^{-1}$ as the jet bulk velocity.

for the DG Tau jet we set $p = 2$, in the present case a better agreement is obtained setting $p = 1$, i.e. for a less steep decrease of the preshock density with distance, i.e. a slower expansion rate for the jet as it propagates into the ambient medium. This can be explained by the higher degree of collimation of the HH 30 jet. A comparison with Paper I shows also that u_0 is lower in this case with respect to the DG Tau parameters, i.e. $u_0 = 50 \text{ km s}^{-1}$ instead of $u_0 = 70 \text{ km s}^{-1}$; this is reflected in the value of the ionization fraction, considerably lower for HH 30. Moreover, we note a higher value of B_0 that must be assumed in the present case with respect to DG Tau. The results are shown in Fig. 3, where we plot the observed line intensity ratios of $[OI]/[NII]$ (bullets) and $[SII]/[OI]$ (circles) (as reported by Bacciotti et al. 1999) and, superimposed, the corresponding model curves ($\langle [OI] \rangle / \langle [NII] \rangle$ dot-dashed line and $\langle [SII] \rangle / \langle [OI] \rangle$ solid line). Since the model proposed is extremely simple, we mainly aim, as shown in Fig. 3, to obtain values of the intensity ratios and trends with distance that are reasonably close to the ones observed, and we cannot account for the knots of emission visible along the HH 30 jet, resulting in ample spatial oscillations of the line intensity ratios, especially in the $[OI]/[NII]$ ratio.

Note also that a different choice of the metal abundances can shift the model lines of Fig. 3 by some percent; e.g. Lodders (2003) reports $N/H = 0.802 \times 10^{-4}$, $O/H = 5.81 \times 10^{-4}$ and $S/H = 1.83 \times 10^{-5}$.

In Fig. 4 we plot the physical parameters that are derived with a special diagnostic technique from observations by Bacciotti et al. (1999) (symbols) compared to the outcome of the present model (lines). We note that the electron density derived

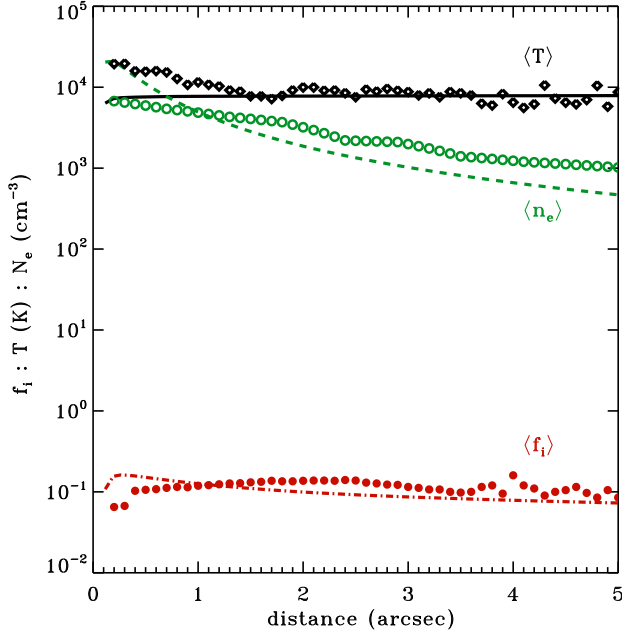


Fig. 4. Average physical parameters of the jet derived from observations following Bacciotti et al. (1999) (symbols) and from the model with *simplified cooling* (curves). Temperature (diamonds, solid line), electron density (circles, dashed) and ionization fraction (bullets, dot-dashed).

from the shock model (dashed line) exceeds the one derived by Bacciotti et al. (1999) (circles) for distances below $\sim 1''$. As discussed in Paper I, however, when the electron density is above the critical density, the ratio of observed [SII] lines, from which n_e is derived, saturates, and the diagnostic in this condition, as reported in the aforementioned paper, yields only lower limits to the electron density. The discrepancy in the electron density affects the diagnostics of temperature (diamonds) that differs from the model one (solid line).

3.2. Detailed cooling

The previous cooling model might be an oversimplified approximation in the case of moderately powerful shocks such as the ones we are dealing with here. This leads to one of the motivations of this paper: a comparative study of the differences between and advantages of each of the two approaches to radiative cooling treatment.

Employing the detailed cooling model, we have explored the parameter space for the same setup as in the previous case. The same method of estimating the root mean square deviation with respect to observations was employed. The best agreement with the observed line intensity ratios was obtained for the following parameters: $n_0 = 5 \times 10^4 \text{ cm}^{-3}$, $B_0 = 500 \mu\text{G}$, $x_0 = 0.''1$, $u_0 = 55 \text{ km s}^{-1}$ and $p = 1$. The resulting line ratios are plotted in Fig. 5 and the evolution of the physical parameters in Fig. 6. In this scheme, the full ionization state of the plasma is computed at each step, allowing for non-equilibrium states. This of course also has a serious impact on the simulation speed, because of the supplementary equations in the system.

The spatial profile of the physical parameters is similar to the one obtained in the best agreement case employing the simpli-

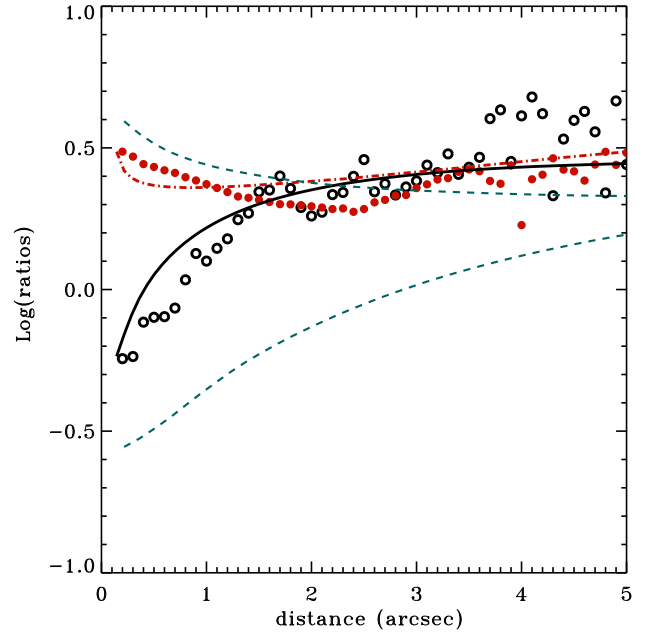


Fig. 5. Intensity ratios of [SII] $\lambda 6716 + \lambda 6731$, [NII] $\lambda 6548 + \lambda 6583$ and [OI] $\lambda 6300$ lines vs distance. Symbols represent the data from Bacciotti et al. (1999) and curves are the computed model curves (with *detailed cooling* treatment): [OI]/[NII] (bullets, dot-dashed line) and [SII]/[OI] (circles, solid line). The model parameters are $n_0 = 5 \times 10^4 \text{ cm}^{-3}$, $B_0 = 500 \mu\text{G}$, $x_0 = 0.''1$ and $u_0 = 55 \text{ km s}^{-1}$, with $U_0 = 95 \text{ km s}^{-1}$ as the jet bulk velocity. The dashed, lighter lines are the results obtained with the simplified cooling model for the same parameter set.

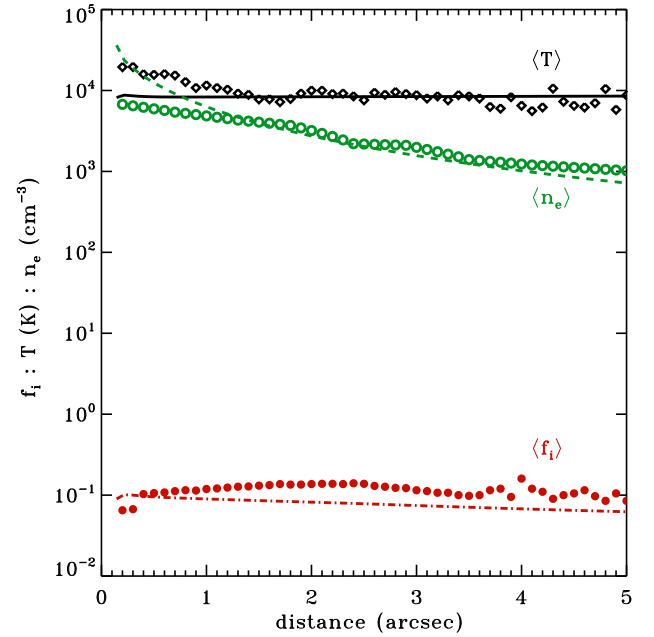


Fig. 6. Average physical parameters of the jet derived from observations following Bacciotti et al. (1999) (symbols) and from the model with *detailed cooling* (curves). Temperature (diamonds, solid line), electron density (circles, dashed) and total ionization fraction (bullets, dot-dashed).

fied cooling. The same considerations of the underestimation of the electron density close to the source apply.

By applying the set of simulation parameters resulting from the simulations with detailed cooling to the setup employing simplified cooling, important differences appear. Due to the higher overall density of the plasma and the much simpler chemistry in the simplified cooling case, the electron density remains at values above the ones derived from observations by a factor of 3 along the evolution of the shock. This is also reflected in the line ratios that depart from the observed ones by a factor of 2 for the $[OI]/[NII]$ and 20% for the $[SII]/[OI]$ ratios, triggered by the higher maximum temperatures attained.

3.3. On the importance of numerical resolution

It is important to understand the resolution needed for these simulations, before moving to 2D configurations (Teşileanu et al. 2009). A rough estimation of the resolution needed in order to resolve the post-shock zone can be done as follows: for a maximum peak temperature of about 10^5 K and densities of $\lesssim 10^5 \text{ cm}^{-3}$, the internal energy density of the gas is of the order of $10^{-6} \text{ erg cm}^{-3}$. According to previous computations (see Teşileanu et al. 2008), the maximum energy loss rate in radiative cooling processes in these conditions is $\sim 10^{-12} \text{ erg cm}^{-3} \text{ s}^{-1}$. Allowing for a maximum relative change in internal energy of 1% in a timestep, the size of the timestep is restricted to about 10^4 s, which combined with the jet velocity of a few hundreds km s^{-1} leads to a space scale of $\sim 10^{11} \text{ cm}$. Even higher resolutions, of a few times 10^{10} cm , are needed to accurately resolve the ionization/recombination processes (with timescales of $\lesssim 10^3$ s). For the setups used in this work, this spatial resolution is attained with 8 levels of refinement.

We have studied the effect of increasing resolution on the line ratios and found it to be important up to a saturation value above which the line ratios do not change significantly. For this, we have computed the root mean square deviations between the simulated values of the line ratios with an increasing number of refinement levels. The results are presented in Table 2, where the first column shows the number of refinement levels in the simulations between which the RMS deviations were computed. Each refinement level doubles the resolution. Three configurations are presented: one with base density $N=2 \times 10^4 \text{ cm}^{-3}$, transverse magnetic field $300 \mu\text{G}$, perturbation amplitude in velocity 50 km s^{-1} ; the second one has $N=5 \times 10^4 \text{ cm}^{-3}$, $B=100 \mu\text{G}$, velocity perturbation 40 km s^{-1} ; the third one has $N=5 \times 10^4 \text{ cm}^{-3}$, $B=500 \mu\text{G}$, velocity perturbation 55 km s^{-1} . The convergence of the results can be inferred from these data.

Sim.	n2e4b300v50		n5e4b100v40		n5e4b500v55	
ref.levs.	R1	R2	R1	R2	R1	R2
base – 2	0.1378	0.0319	0.1240	0.0477	0.1150	0.0477
2 – 4	0.0512	0.0171	0.0883	0.0534	0.0884	0.0499
4 – 6	0.0141	0.0816	0.0425	0.0418	0.0589	0.0509
6 – 8	0.0110	0.0141	0.0088	0.0145	0.0256	0.0359
8 – 10	0.0004	0.0008	0.0017	0.0023	0.0033	0.0084

Table 2. Root mean square deviations of line ratios (R1 is $[OI]/[NII]$, R2 is $[SII]/[OI]$) obtained with simulations of increasing resolution.

Presented in Fig. 7 are four cases of increasing resolution for the first configuration in Table 2 (n2e4b300v50): one employing

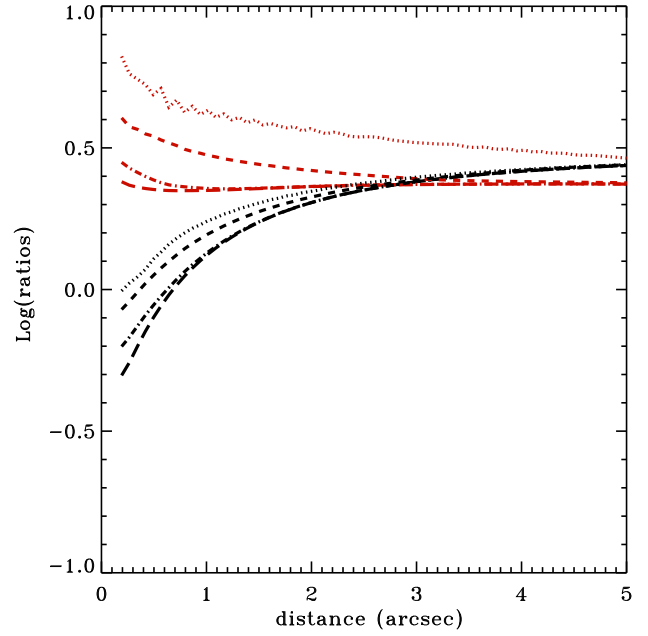


Fig. 7. Effect of the simulation resolution on the line ratios of $[SII]\lambda 6716 + \lambda 6731$, $[NII]\lambda 6548 + \lambda 6583$ and $[OI]\lambda 6300$ lines, in the case of *simplified cooling*. The setup is identical to the one in Fig. 3, with the four line sets representing results from simulations with 10 levels of refinement (long-dashed lines), 6 levels of refinement (dash-dotted lines), 3 levels of refinement (dashed lines) and without refinement at all (dotted lines), respectively.

only the base grid (1 536 zones), a second one with three levels of refinement (equivalent resolution 12 288 cells), one using six levels of refinement (equivalent resolution 98 304 cells), and one with 10 levels of refinement (equivalent resolution 1 572 864 cells). It can be seen that the line ratios converge to the results of Fig. 3, obtained in a simulation with 8 levels of refinement. The simulations presented in Fig. 7 use the simplified cooling model, but similar effects were obtained when using the detailed cooling model. In Fig. 7, the line ratios obtained employing 8 levels of refinement almost perfectly overlapped the ones obtained with 10 levels of refinement, so they were not shown.

The physical spatial resolution in a simulation with 8 levels of refinement in the present setup is about $1.2 \times 10^{10} \text{ cm}$, and should be enough to adequately resolve the post-shock zone, with its rapid variation of physical parameters. The resolution for 6 levels of refinement is $\sim 5 \times 10^{10} \text{ cm}$, it drops to $4 \times 10^{11} \text{ cm}$ for three levels of refinement and to $3.25 \times 10^{12} \text{ cm}$ at the base grid resolution.

The line ratios are very sensitive to resolution variations, making it important to reach an adequate (high) resolution for reliable results. This is a critical aspect for future 2D simulations, that will have to employ AMR to reach these extremely high resolutions with the available computational power.

In order to see how the resolution requirements depend on the parameters of the shock, in Fig. 8 we present the evolution of the temperature at the same age for three shockwaves with different amplitudes of the initial perturbation (decreasing from left to right). The x axis does not represent the actual position of the shocks but only a distance scale, the front of the shockwaves being plotted close to each other for convenience. We see that with the increase of the perturbation amplitude (and thus the

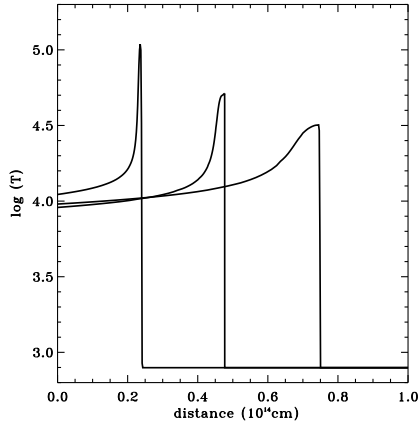


Fig. 8. Three simulations of shockwaves with density $N=2 \times 10^4 \text{ cm}^{-3}$, transverse magnetic fields $300 \mu\text{G}$, and perturbation amplitudes in velocity of (from left to right) 70, 50 and 40 km s^{-1} , respectively, at the same evolutionary point. Logarithmic plots of temperature.

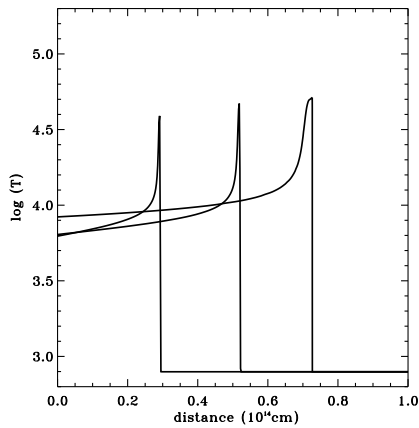


Fig. 9. Three simulations of shockwaves with transverse magnetic fields $300 \mu\text{G}$, perturbation amplitude in velocity of 50 km s^{-1} , and base densities of (from left to right) 8, 5, and $2 \times 10^4 \text{ cm}^{-3}$, respectively, at the same evolutionary point. Logarithmic plots of temperature.

shock strength), the evolution after the shock steepens. In the same way, in Fig. 9 three shockwaves with different initial densities are plotted, with decreasing density from left to right. The evolution of the temperature after the shock steepens when increasing the density. Typically, as the dependence steepens, the resolution needed increases. All the cited plots were made for the same average velocity of the underlying jets. When decreasing this velocity, the spatial resolution needed for an accurate analysis of the post-shock zone increases.

3.4. Comparison and discussion

The parameter sets for the best agreement obtained in the previous paragraphs were not the only ones that well interpret the observations, but other possible “successful” combinations do not depart from these values of the parameters. As an example, setting $U_0 = 95 \text{ km s}^{-1}$ for the bulk jet velocity, we obtained model

curves very similar to those of Figs. 5 and 6 with the same $p = 1$, $x_0 = 0.1$ but with $n_0 = 4 \times 10^4 \text{ cm}^{-3}$, $B_0 = 300 \mu\text{G}$, and $u_0 = 58 \text{ km s}^{-1}$. The same considerations apply for the simplified cooling simulations.

The jet bulk speeds U_0 were chosen in such a way that the total shock speed in the rest reference frame would be approximately equal to 150 km s^{-1} in all cases – this being an approximate average knot speed derived from observations of Doppler shifts and proper motions (Hartigan & Morse 2007).

Comparing the results obtained with the two approaches to radiative cooling, identical or similar values of the model parameters can be inferred (Table 3). Parameters such as velocity amplitude of the perturbation (determining the shock strength) and transverse magnetic field (resulting in shock compression) are similar in the two cases. The total density of the jet is however one of the most difficult parameters to estimate from observations, and the different results in our two cases come from the different evolution of the total radiative losses and ionization in the post-shock zone.

Parameter	Simplified	Detailed
$n_0 (\text{cm}^{-3})$	2×10^4	5×10^4
$B_0 (\mu\text{G})$	300	500
$u_0 (\text{km s}^{-1})$	50	55
$U_0 (\text{km s}^{-1})$	100	100
$f_i (\%)$	0.1	0.1
$T_0 (\text{K})$	1000	1000

Table 3. Comparison of the model parameters that gave the best agreement with the observations of HH30.

The simplified radiative cooling treatment appear to be suited for a rapid exploration of the parameter space, giving results (parameters of the model) close to the ones obtained with more sophisticated cooling.

4. Conclusions and summary

We have demonstrated in previous works that numerical integration of time-dependent radiating (shocked) flows can substantially benefit from the employment of adaptive mesh refinement methods, and the present work supports this conclusion. By computing the cooling time scale according to the algorithm described in Mignone et al. (2009), one could take full advantage of the time adaptation process. The use of this method allows us to tackle simulations of radiating shocks in 2D as they propagate along a cylindrical supersonic jet.

Our results applied to the DG Tau jet (Paper I) as well as the HH 30 jet (present paper) revealed a good agreement between the observed and calculated line intensity ratios of different transitions and for different elements (Figs. 3 and 5), and also of derived physical parameters, including the ionization fraction (Figs. 4 and 6).

An accurate treatment of the radiative losses allows us to more realistically compute the full ionization state of the plasma, and thus accurate line emission for each ion, in the approximation of a five-level atom. This, however, requires significant additional computing power that is not always available. An alternative is the use of the simplified cooling model, following only the ionization state of hydrogen, that proved to give good indications on the perturbation amplitude and transverse magnetic field of our model. This simpler but much faster strategy may be

used for a preliminary exploration of the parameter space, being followed by simulations with detailed cooling only in the areas of interest. Both cooling models were discussed and compared in Teşileanu et al. (2008), and in the present work we extended the comparison to line ratio diagnostics and application to a real HH object.

Grid resolution proved to be a critical parameter for the line ratios estimations from MHD simulations. The physical dimensions of the computational zones have to not exceed about 10^{11} cm in order to accurately capture the evolution of the physical parameters and emission properties in the post-shock zones. This is a crucial aspect for future 2D simulations that will have to fulfill these requirements. This result can be generalized for the typical conditions encountered in shocks traveling through protostellar jets, as the variability in these conditions could not change the numbers by an order of magnitude. Weaker shocks (shocks evolving from smaller initial perturbations) or lighter shocks (lower initial density) will be less stringent on the resolution requirements, while stronger and/or denser shocks will add a factor to the present results.

We can summarize the general picture as follows: i) when one is interested in the distribution in space of the jet physical parameters such as density, temperature, etc., the details of the assumed cooling function matter very little (Teşileanu et al. 2008) provided the numerical resolution suffices to minimize numerical dissipation effects; ii) when one considers the detailed shock structure, numerical resolution is more important, but less so for the behavior of the integrated emission line luminosities (Raga et al. (2007)); iii) when one discusses the line intensity ratios, a finer resolution must be achieved, while the details of the cooling function have effects that differ according to the line considered, in the present case from about 10% up to a factor of two.

Acknowledgements. We acknowledge the Italian MIUR for financial support, grants No. 2002.028843 and No. 2004.025227. The present work was supported in part by the European Community Marie Curie Actions - Human resource and mobility within the JETSET network under contract MRTN-CT-2004 005592. OT acknowledges the support from the Romanian Research Agency CNCSIS, contract number RP-4/2009. We thank the anonymous referee for valuable observations and suggestions.

References

- Bacciotti, F., Eislöffel, J., Ray, T. P. 1999, A&A 350, 917
 Berger, M. J., Colella, P. 1989, Journal of Computational Physics, 82, 64-84
 Berger, M. J., Olinger, J. 1984, Journal of Computational Physics, 53, 484-512
 Cox, D., Raymond, J. 1985, ApJ 298, 651
 Garcia, P. J. V., Ferreira, J., Cabrit, S., Binette, L. 2001a, A&A 377, 589
 Garcia, P. J. V., Cabrit, S., Ferreira, J., Binette, L. 2001b, A&A 377, 609
 Hartigan, P., Morse, J. A., Raymond, J. 1994, ApJ 436, 125
 Hartigan, P., & Morse, J. 2007, ApJ 660, 426
 Hyman, J.M. 1983, SIAM J. Sci. Stat. Comput., 4(4), 645-654
 Lavalley-Fouquet, C., Cabrit, S., Dougados, C. 2000, A&A 356, L41
 Lodders, K. 2003, ApJ 591, 1220
 Lohner, R. 1987, Comp. Meth. App. Mech. Eng., 61, 323
 Massaglia, S., Mignone, A., Bodo, G., 2005a, A&A 442, 549 (Paper I)
 Massaglia, S., Mignone, A., Bodo, G. 2005b, Mem.S.A.It. 76, 378
 Mignone, A., et al. 2009, in preparation
 Mignone, A., Bodo, G., Massaglia, S., Matsakos, T., Teşileanu, O., Zanni, C., Ferrari, A. 2007, ApJS, 170, 228
 O'Brien, D., & Garcia, P. 2003, APSS 287, 3
 Osterbrock, D.E., & Ferland, G.J. 2006, *Astrophysics of Gaseous Nebulae and Active Galactic Nuclei*, 2nd ed., University Science Books, Sausalito - California
 Raga, A. C., De Colle, F., Kajdič, P., Esquivel, A., Cantó, J. 2007, A&A 465, 879
 Shang, H., Glassgold, A.E., Shu, F. H., Lizano, S. 2002, ApJ 564, 853
 Strang, G. 1968, SIAM J. Num. Anal., 5, 506
 Teşileanu, O., Mignone, A., Massaglia, S. 2008, A&A 488, 429

Teşileanu, O., Mignone, A., Massaglia, S. 2009, Procs. "Protostellar Jets in Context", T.P. Ray & K. Tsinganos eds., 7-12 July 2008, Rhodes, Greece, Springer, in press